Sensors & Actuators: A. Physical 363 (2023) 114729

Contents lists available at ScienceDirect

Sensors and Actuators: A. Physical

journal homepage: www.journals.elsevier.com/sensors-and-actuators-a-physical

A heat flux sensor leveraging the transverse Seebeck effect in elemental antimony

Kenneth McAfee [a], Peter B. Sunderland [b], Oded Rabin [c,d,*]

[a] Department of Aerospace Engineering, University of Maryland, College Park, MD 20742, USA
[b] Department of Fire Protection Engineering, University of Maryland, College Park, MD 20742, USA
[c] Department of Materials Science and Engineering, University of Maryland, College Park, MD 20742, USA
[d] Institute for Research in Electronics and Applied Physics, University of Maryland, College Park, MD 20742, USA

ARTICLE INFO

Keywords:
Heat flux sensor
Thermoelectrics
Transverse Seebeck effect
Antimony
Single crystal
Anisotropy

ABSTRACT

Certain configurations of anisotropic single crystal materials can generate a thermoelectric voltage orthogonal to an induced temperature gradient. This phenomenon is known as the Transverse Seebeck Effect (TSE) and can be leveraged to fabricate simple and robust heat flux sensors. Only a small number of materials have been considered as TSE-based transducers and, among these, few have been developed into sensors with ruggedization against chemical and mechanical degradation. Here, we report on the fabrication and characterization of a rugged TSE-based heat flux sensor using prismatic antimony single crystals. The heat flux sensor was tested under static and dynamic heating scenarios. The sensor has a linear responsivity of 16.8 μV/(W/cm^2) to heat fluxes spanning more than two orders of magnitude and a time constant of 4.4 s. The sensor's response to localized heating, probed with a laser scanning technique, validated that the transduction mechanism is primarily the TSE by ruling out a sizable contribution from the conventional Seebeck effect. Finite element analysis corroborated that components used in the sensor package are the primary determinants of the time constant and the decrement of the responsivity from its theoretical maximum. Design principles that may be applied to elicit a faster transient response or higher responsivity are proposed. The results establish single crystal antimony as a promising transducer material for heat flux measurement systems and demonstrate potential effects of ruggedization on sensor performance.

1. Introduction

Solid state devices for direct heat flux measurements typically rely on thermoelectric effects [1]. Among these, many heat flux sensors, such as Gardon and Schmidt-Boelter gauges, determine heat flux using the conventional Seebeck effect (CSE). As heat flows into the device, a temperature difference established between two dissimilar material junctions produces a thermoelectric voltage. This voltage is a function of the difference in the Seebeck coefficients of the materials, the temperature difference between junctions, and the number of serial junctions present [2]. Alternatively, heat flux sensors can utilize the transverse Seebeck effect [3,4]. The transverse Seebeck effect (TSE) is a phenomenon whereby a voltage is generated perpendicular to a temperature gradient in an anisotropic material [5], as illustrated in Fig. 1 for an anisotropic single crystal. Assuming a uniform temperature gradient in the $\hat{z}$-direction in Fig. 1, the voltage measured along the $\hat{x}$-direction V_x due to the TSE is given by Eq. 1 [6].

$$V_x = (S_{CP} - S_{IP}) \sin\theta \cos\theta \frac{q_z}{k} L \quad (1)$$

Here, S_{IP} and S_{CP} are the in-plane (IP) and cross-plane (CP) components of the anisotropic Seebeck coefficient tensor, respectively, θ is the inclination of the anisotropic material with respect to laboratory coordinates, k is the thermal conductivity (assumed isotropic), and L is the length between voltage measurement points. q_z is the heat flux parallel to the $\hat{z}$-axis and is related to the temperature gradient $\partial T/\partial z$ by Eq. 2.

$$q_z = -k\frac{\partial T}{\partial z} \quad (2)$$

Devices using the TSE only require a single transducer material to generate a voltage output, in contrast with a pair of materials required for CSE sensors. The voltage can be scaled up by increasing the overall length of the transducer or connecting multiple in series. Furthermore,

* Corresponding author at: Department of Materials Science and Engineering, University of Maryland, College Park, MD 20742, USA.
E-mail address: oded@umd.edu (O. Rabin).

https://doi.org/10.1016/j.sna.2023.114729
Received 25 July 2023; Received in revised form 27 September 2023; Accepted 4 October 2023
Available online 5 October 2023
0924-4247/

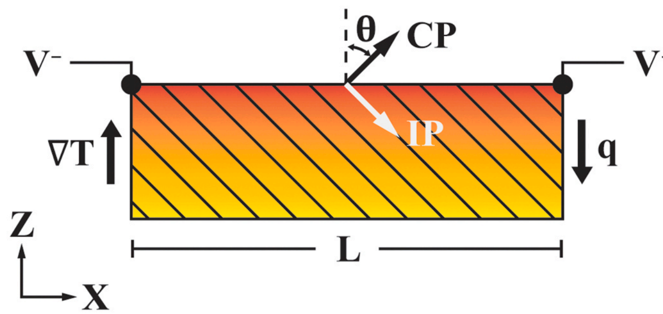

Fig. 1. Schematic of a TSE transducer. A $\hat{z}$-axis oriented temperature gradient ∇T induced by a heat flux q generates a perpendicular voltage difference $V^+ - V^-$ along the $\hat{x}$-axis. The voltage difference is a function of the length L and inclination θ of the anisotropic single crystal, denoted here with in-plane (IP) and cross-plane (CP) crystallographic axes.

the contributions to the signal from the thermopower of the electrical wiring material are negligible, as all electrical wire/transducer contacts are at identical temperatures. These advantages allow for heat flux sensors using the TSE to exhibit simpler and more robust constructions [7].

Investigations of the TSE have employed anisotropic single crystals [5,8–10], layered composites [11–17], or have utilized the magnetization of the material to induce anisotropy [18–21]. For the construction of heat flux sensors, the latter approach is highly inconvenient. Layered composites can be engineered as superior TSE transducers over naturally occurring crystals [22], however, special precautions must be taken to prevent intermixing of the components and a drift in sensor characteristics [23]. Single crystals are thus the most common type of transducer used in TSE-based heat flux sensors. Prior art includes sensors using bismuth [8], Bi_2Te_3 [24], and $YBa_2Cu_3O_{7-d}$ and other layered oxides [5,6,25–31], the latter primarily investigated as thin films for high speed sensing.

Here, the TSE in single crystal antimony is demonstrated as a practical heat flux transduction mechanism in a sealed and robust heat flux sensor. The sensor design and fabrication is discussed in Section 2, with an emphasis on the structural components used to ruggedize the sensor. While earlier TSE-based heat flux sensors have been used without a robust sealed package, these components are essential for protection from chemical and physical damage, albeit at the cost of impairing the flow of heat through the transducer. Section 3 details the characterization of the sensor subject to a uniform steady heat flux and introduces an analytical model coupled with finite element analysis (FEA) simulations to predict the sensor's theoretical responsivity. Section 4 details the characterization of the sensor subject to transient heating and analyzes the impact of the package design parameters on the time constant via FEA. The sensor's response to a localized heat source is discussed in Section 5, including observations of a TSE-dominated response under experimental conditions favorable to a combined TSE and CSE response.

2. Heat flux sensor design and fabrication

The sensor components are shown in Fig. 2, with component material properties summarized in Table 1. The components include two prismatic antimony transducers, the ceramic housing, two auxiliary thermocouples, wiring, and the heat spreading cover plate. Two transducers measuring 5.1 × 2.1 × 1.45 mm were sectioned using a dicing saw from a cylindrical antimony single crystal pellet (Goodfellow Corp., purity 99.999%, diameter 11 mm, height 2.1 mm, axis orientation: [11$\bar{2}$0]). To obtain the crystal orientation which maximizes the TSE (Eq. 1), dicing planes were at a 45° angle to both the [0001] and [1$\bar{1}$00] crystallographic directions. The ceramic housing (Boron Nitride PCBN1000, Precision Ceramics USA Inc.) was machined to outer

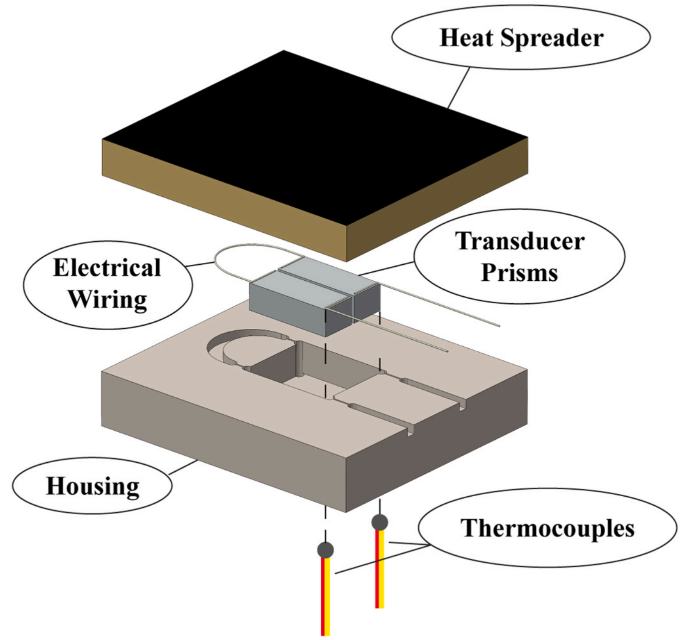

Fig. 2. Exploded view of the sensor. The front end is a painted brass heat spreader, fixed over the ceramic housing which accommodates two prismatic antimony transducers and tungsten wires. Two auxiliary thermocouples that probe the temperature at two antimony/tungsten junctions extend from the back end.

Table 1
Summary of material parameters for the TSE heat flux sensor.

Property	Value at room temperature	Reference
Brass, thermal cond.	1.16 W/(cm-K)	
Ceramic, thermal cond.	0.21 W/(cm-K)	
Cement, thermal cond.	0.033 W/(cm-K)	
Antimony, thermal cond.	0.22 – 0.244 W/(cm-K)	[32,33]
Antimony, Seebeck coeff.	S_{11} = 44 μV/K, S_{33} = 21 μV/K	[32]
Antimony, resistivity	44 μΩ-cm	This work
Tungsten wire, Seebeck coeff.	-0.12 μV/K	This work
Tungsten wire, resistivity	6 μΩ-cm	This work
Resistance of sensor	8 – 16 Ω	This work

dimensions of 16 × 14 × 3 mm. PCBN1000 was chosen as the housing material because its thermal conductivity is similar to that of antimony, minimizing the housing's impact on the heat flow through the transducers. The transducers were mounted in a cavity, 5.4 × 4.5 × 1.75 mm, milled into the ceramic housing using cement (Sauereisen TempSeal Cement No. 3). Tungsten wires (McMaster-Carr, 99.95%, 0.2 mm) were attached to the prisms using PELCO colloidal silver (Ted Pella 16034). Two auxiliary 40 AWG type-K thermocouples (Omega Engineering 5SC-TT-K-40–36-ROHS) were attached near the contacts between the tungsten wires and the transducers. The gaps between the transducers and the housing were filled with cement. Cement was also used to attach the brass heat spreading cover plate (McMaster-Carr, ultra-Machinable 360 Brass), measuring 16 × 14 × 2 mm, to the corresponding face of the ceramic housing near the transducers. Fig. 3 shows the sensor before and after attaching the brass plate. The outward facing surface of the brass plate was spray-coated with high temperature black paint (Rust-Oleum 248903). This black face is the heat flux-facing end of the sensor (i.e., front end). On the back end of the sensor, a water-cooled heat sink was attached. The interface between the sensor and the heat sink was filled with thermal compound (MX-5, ARCTIC) to improve heat dissipation. The free ends of the tungsten wires were connected to the electrical leads of a nanovoltmeter (Keithley 2182A). The auxiliary thermocouples were connected to a data acquisition module (Pico

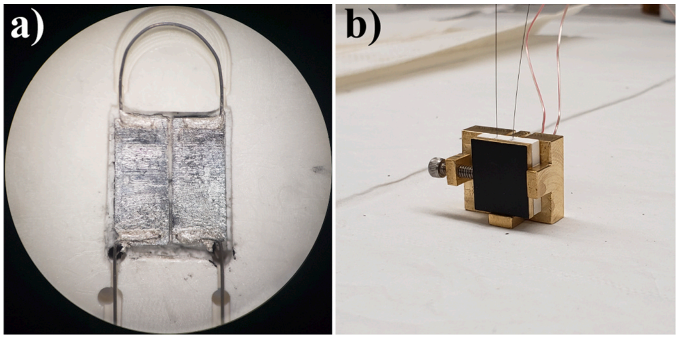

Fig. 3. (a) Optical microscope image of the sensor before attaching the brass plate. (b) Completed sensor mounted on a brass holder.

Technology TC-08). The as-built heat flux sensor measured 16 × 14 × 5.3 mm with a frontal area of 224 mm^2.

3. Steady state sensor characterization

3.1. Steady state response

The heat flux sensor was calibrated against a reference gauge using a transfer calibration technique [34,35]. In this method, the response of the TSE sensor is compared to the response of the reference gauge with both sensors exposed sequentially to an identical heat flux. A NIST-traceable Schmidt-Boelter gauge (Medtherm 64–3–20) was used as the reference gauge. Two different radiative heat sources, a propane heater and a blackbody furnace (Oriel 67032), were used during the calibration campaign. The separation between the heat source and the gauges was varied from 1 to 100 cm to produce a range of heat fluxes. The furnace temperature was adjusted to achieve heat fluxes up to 7 W/cm^2.

The sensors were mounted on a translation stage that allowed for repeatable positioning (within 0.05 cm) of each sensor at the same location in the line-of-sight of the heat source. Once the heat source setpoint was established, a sensor was positioned in line-of-sight. The other was positioned behind a reflective barrier. After 60 – 90 s, when a steady signal was achieved, the sensor positions were interchanged. Three repeat measurements were performed and averaged for each sensor.

The front surface temperature of each sensor and the ambient temperature were monitored during the calibration. To account for differences in convective heat flux from the ambient environment to each sensor, the total measured heat flux q_{in} due to both convective and radiative heating (Eq. 3) was considered in the calibration.

$$q_{in} = \alpha\, q_{rad} + h(T_\infty - T_s) \tag{3}$$

In Eq. 3, α is the absorptivity of the sensor surface, q_{rad} is the incident radiative heat flux, h is the convective heat transfer coefficient, and T_∞ and T_s are the ambient and sensor surface temperatures, respectively. The absorptivity of both sensor surfaces is estimated as $\alpha \cong 0.95$ [36], thus the radiative heating term in Eq. 3 is equal for both sensors. The convective heat transfer coefficient, given in W/(cm^2-K), was approximated using Eq. 4, which is based on empirical parameters determined from an analogous propane heater calibration setup and Schmidt-Boelter heat flux sensor [37].

$$h = 0.00078(T_\infty - T_s)^{0.36} \tag{4}$$

Combining Eqs. 3 and 4, the total heat flux measured by the TSE sensor can be expressed as

$$q_{in,TSE} = q_{in,ref} + 0.00078\left[(T_\infty - T_{s,TSE})^{1.36} - (T_\infty - T_{s,ref})^{1.36}\right] \tag{5}$$

where the subscripts *TSE* and *ref* are used to denote parameters of the TSE and reference sensors, respectively. $q_{in,ref}$ was determined from the averaged reference sensor voltage using the manufacturer supplied calibration curve. The maximum difference in convective heat flux between the TSE and reference sensors was 7% of $q_{in,ref}$.

A total of 105 data points were used to construct the sensor calibration curve in the range of 0 – 7 W/cm^2 (Fig. 4). A straight line was fit to the data, yielding a sensor responsivity (i.e., slope) of 16.8 μV/(W/cm^2) with a 95% confidence interval of 16.7 – 17.0 μV/(W/cm^2), assuming normally distributed measurement errors. The sensor response is linear from 0.06 to 7 W/cm^2, with the upper limit of the calibration restricted by the design limits of the Medtherm reference sensor. At equilibrium without incident heat flux, the TSE sensor's baseline voltage offset is 0.080 μV, corresponding to a detection threshold of 5×10^{-3} W/cm^2.

Throughout the calibration campaign, spanning four months, no change was observed in the responsivity, demonstrating good stability of the TSE sensor. This stability may be attributed to the fact that the temperature of the sensor never exceeded the maximum temperature used during assembly (100 °C, while curing the black paint). At the high end of heat fluxes tested, the sensor was exposed to ambient temperatures of up to 350 °C, however, the interior temperature, probed by the auxiliary thermocouples, did not exceed 74 °C due to the water-cooled heat sink.

3.2. Analysis of the sensor's steady-state response

In single crystal antimony, the Seebeck coefficient anisotropy $|S_{33} - S_{11}|$ and thermal conductivity (which is nearly isotropic) have been reported in the range of 23 – 26 μV/K [32,38] and 0.22 – 0.24 W/(cm-K), respectively. The transducers were fabricated in the optimal orientation of $\theta = \pi/4$ to maximize the TSE. Following Eq. 1, the theoretical responsivity of the single crystal antimony transducer is at least 52.5 μV/(W/cm^2) per cm length between voltage contacts.

Eq. 1, however, may only be applied if the heat flux through the transducers is parallel to the $\hat{z}$-axis. In practice, this cannot be perfectly satisfied in a multi-component/multi-material device. Lateral heat flows within the sensor induced as a result of its design have two important consequences: (I) heat flux components perpendicular to q_z will arise within the transducers thereby reshaping the voltage distribution via the TSE and CSE, and (II) the average value of q_z within the transducers will vary compared to the value of q_{in} incident on the front surface of the

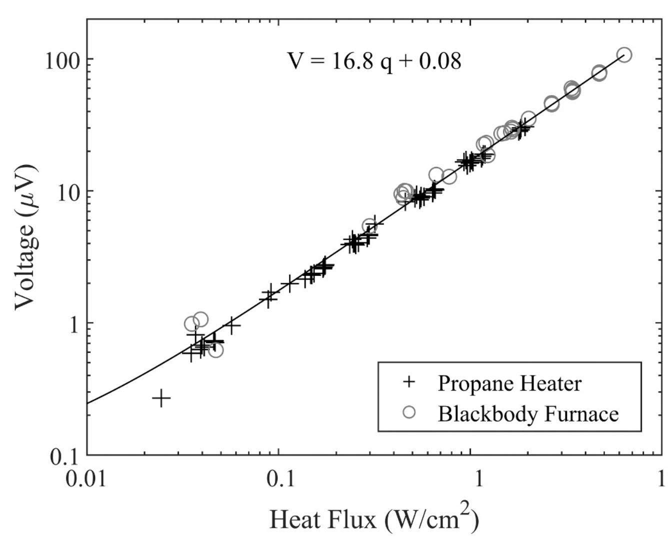

Fig. 4. Experimental calibration curve for the TSE-based antimony heat flux sensor. Data sets obtained with different radiative heat sources are overlayed. The linear fit using the totality of data is displayed as a solid line, with the corresponding equation shown in the plot.

sensor. Generally, V_x will remain proportional to q_{in}, however the responsivity will deviate from Eq. 1 due to the augmentation or attenuation of the average value of q_z and CSE contributions within the transducers. Therefore, it is crucial to consider the impact of the design and materials selection for each component of the sensor on the heat flow in and around the transducers. When considering the as-built sensor holistically,

$$V_x = 52.5\ \epsilon\ q_{in}\ L \tag{6}$$

where q_{in} is the incident uniform heat flux on the front surface of the sensor and ϵ is the gain defined as the ratio of the average $\hat{z}$-component heat flux within the volume of the transducers to the incident heat flux:

$$\epsilon = \frac{mean(q_z)}{q_{in}} \tag{7}$$

The value of ϵ was established using finite element analysis simulations (ANSYS APDL). A model of the sensor was generated utilizing the as-built sensor geometry and the corresponding material properties. The model was subjected to boundary conditions that mimic the conditions in the laboratory, as illustrated in Fig. 5a: A uniform heat flux q_{in} was imposed on the front surface of the heat spreader and the back surface of the ceramic housing was held at a constant temperature. Nodal solutions of q_z within the volume of the transducers were extracted from the ANSYS steady-state thermal analysis solution to determine the gain, with each nodal solution of q_z weighed proportional to the average volume of adjacent elements to account for the non-uniform mesh density. For the as-built sensor, a gain of 0.70 – 0.85 was found, with the range of values accounting for uncertainties in the cement properties. As the thermal conductivity of the package and transducer components are similar, the low gain is primarily attributed to the low thermal conductivity of the cement layers on the front and back of the transducers. The streamlines in Fig. 5b show the simulated magnitude and direction of the heat flux along the $\hat{y} - \hat{z}$ symmetry plane in the center of the sensor. The streamlines deflect from the vertical path to avoid the additional thermal resistance imposed by the excess thickness of the cement layers in the center region. The heat flux entering the transducers is lower (green in Fig. 5b) and that entering the housing is higher (orange) compared to the heat flux entering the brass (yellow).

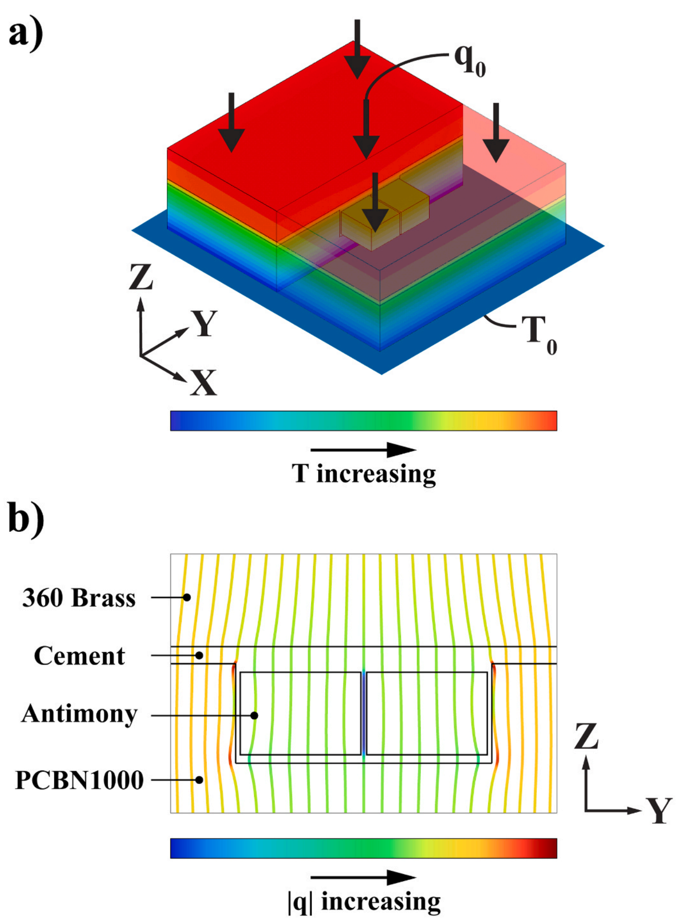

Fig. 5. Steady-state finite element simulations. a) Temperature contour map of the finite element model. A uniform heat flux q_0 is imposed on the top surface and the bottom surface is held at a constant temperature T_0. b) Heat flux streamlines on the $\hat{y} - \hat{z}$ symmetry plane through the center of the model. The streamline colors represent the magnitude of heat flux. The boundaries between the components are superimposed as black lines.

Taking into account the attenuation of the heat flux through the transducer relative to q_{in}, the responsivity is predicted to be 30 – 37 μV/(W/cm^2) for a total length of 0.82 cm between voltage contacts (Eq. 6). The measured value of 16.8 μV/(W/cm^2) is lower, with the decrement attributed to an overestimation of the black paint absorptivity, imperfections in the construction of the sensor, and uncertainty in the Seebeck coefficient tensor components. Contributions from the CSE were ruled out by monitoring the temperature near the transducer/electrical wire junctions using the embedded auxiliary thermocouples. The impact of temperature gradients along the $\hat{x}$-axis were deliberately minimized by using two identical transducers, as shown in Fig. 3a, where the crystallographic orientations are related by a 180° rotation around the $\hat{z}$-axis. As such, q_z-related transverse Seebeck voltages generated in the two prisms add together, while equal and opposite CSE voltages offset, as illustrated in Fig. 6 [7,8].

The dependence of the responsivity of heat flux sensors on temperature has been the subject of many studies [2,39–41]. In these thermopile-based sensors, responsivity values have been shown to vary by 10% [39] and 14% [41] from room-temperature to 80 °C. In TSE-based sensors, the temperature-dependence of the responsivity contains two main contributions: (I) the transducer material properties which appear in Eq. 1 and (II) the gain of the sensor (Eqs. 6 and 7). According to literature data, the Seebeck coefficient tensor anisotropy [42] and the thermal conductivity [32,33] of single crystal antimony increase and decrease, respectively, as the temperature increases from room temperature. This contribution is predicted to increase the responsivity by 12% when the sensor temperature is raised from 19 °C to 74 °C (upon exposure to 7 W/cm^2, with water cooling), and should result in a nonlinear convex calibration curve. The data in Fig. 4, however, suggests a much lower variation in the responsivity. This is likely because the increase in transducer responsivity is offset by a decrease in sensor gain over the same temperature range. The lower gain is a result of a decrease in the thermal conductivity of antimony relative to the thermal conductivity of the ceramic housing, diverting a larger portion of the heat flux away from the transducers.

4. Transient sensor characterization

4.1. Transient response

The transient response of the heat flux sensor was analyzed by subjecting the sensor to a step change in heat flux. The blackbody furnace, held at 1000 °C, was used as the heat source. The heat flux sensor was positioned in the furnace line-of-sight at a distance of 15 cm. The step change in heat flux was achieved using a reflective shield 7.5 cm from the furnace which could be quickly removed. The sensor voltage and temperature data were recorded at 5 Hz. Following each step change, the signals were allowed to reach steady-state. The shield was inserted and removed four times.

A representative plot of voltage versus time delay for four transients is shown in Fig. 7. The time constant τ is defined as the rise time for the sensor to reach 63.2% of the steady-state voltage. The average value of τ

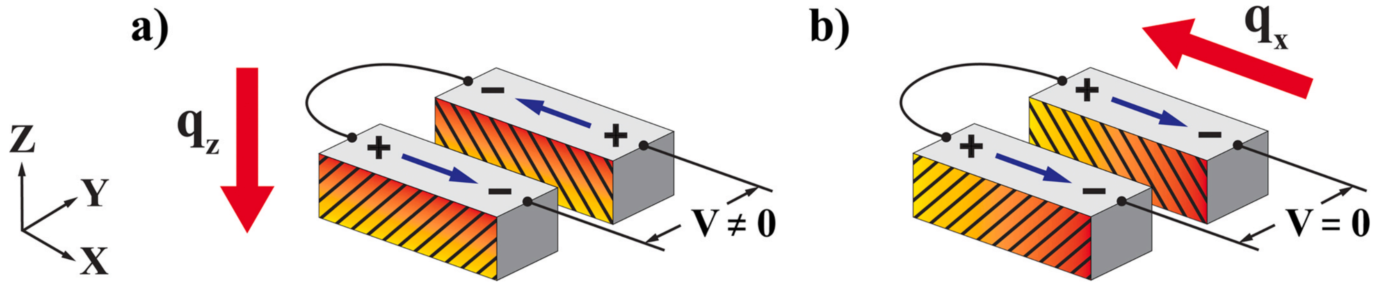

Fig. 6. Illustration of the polarity of the Seebeck voltage along the $\hat{x}$-axis (sign symbols and blue arrows) in a pair of transducers with crystallographic tilt angles of $+\theta$ and $-\theta$ about the $\hat{y}$-axis, respectively (parallel hatching). The heat flux is represented by a red arrow and the temperature gradient by a color gradient, as in Fig. 1. (a) Heat flux q_z induces a temperature gradient along the $\hat{z}$-axis and generates transverse Seebeck voltages with opposite polarities. The voltages add up along the circuit loop. (b) Heat flux q_x induces a temperature gradient along the $\hat{x}$-axis and generates Seebeck voltages with equal polarities. The voltages offset each other along the circuit loop.

for the TSE heat flux sensor was 4.4 ± 0.3 s. Under the same conditions, the time constant of the reference Medtherm 64–3–20 heat flux sensor was 0.45 ± 0.1 s. The time constant was independent of the value of the heat flux.

4.2. Analysis of the sensor's transient response

The transient response of a heat flux sensor is dependent on the position of the transducers within the housing and the materials used in the sensor construction. In the TSE sensor, the transducers are placed behind a high thermal conductivity heat spreader and a low thermal conductivity cement layer, and are separated from the water-cooled heat sink by a ceramic housing. Transient finite element simulations were conducted to evaluate the influence of these components on τ. In these simulations, a step change in heat flux was imposed on the front surface of the heat spreader, and a constant temperature was imposed on the back surface of the ceramic housing. The heat spreader characteristics had the largest impact on τ [43]. The time constant is linearly proportional to the product of its thickness and specific heat, all other parameters unchanged. The thermal conductivity of the heat spreader has an insignificant effect. τ is only weakly impacted by the thermal properties of the cement and the ceramic components. With the temperature constrained at the back surface of the lower thermal conductivity ceramic housing, the transient response is dominated by the time needed for the temperature to rise at the front of the sensor. This rise time is governed by the thermal mass of the heat spreader, i.e., the product of its volume, density, and specific heat. As an experimental confirmation, an applied heat flux step of 0.79 W/cm^2 caused the temperature near the front of the transducers to rise by 5.2 K. With a thermal mass per area of 0.714 (J/K)/cm^2, the heat spreader temperature would increase by 5.2 K in 4.8 s when losses are ignored, in good qualitative agreement with the experimental time constant. If shorter response times are required, the design can be modified using a thinner, lower thermal mass heat spreader.

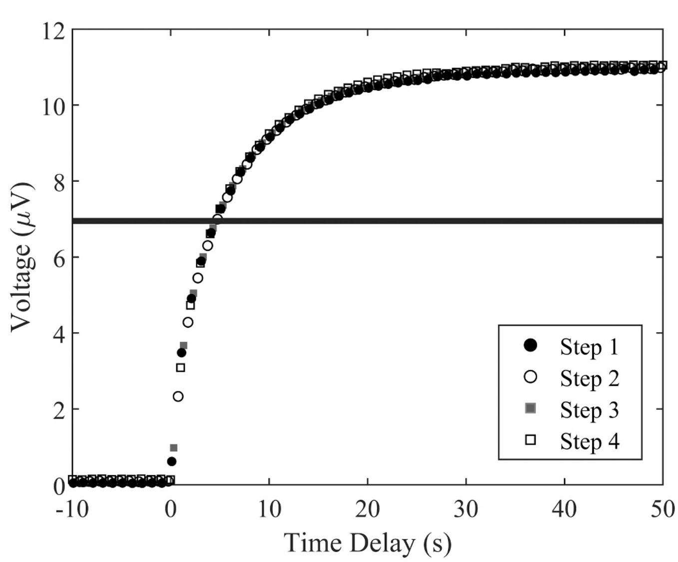

Fig. 7. Transient response of the antimony TSE-based heat flux sensor to a step change in heat flux. The horizontal line indicates the signal corresponding to 63.2% of the steady-state voltage. The intersection between the voltage transient and the horizontal line was used to determine the time constant of the sensor ($\tau = 4.4$ s).

5. Sensor response to localized heating

A laser scanning technique was used to stimulate the heat flux sensor with a localized heat probe that produced temperature gradients both normal and parallel to the front surface of the sensor. A 808 nm continuous-wave diode laser with an optical power of 156 mW and a 2 mm beam diameter was utilized as the heat source. The location of the beam incident on the front face of the sensor was controlled using a translation stage. The laser beam was scanned at normal incidence across a 10.2 × 7.6 mm area near the center of the heat flux sensor. The sensor's steady-state voltage was recorded for 195 discrete locations. Fig. 8 summarizes the results of the laser scan experiment. Notably, in Fig. 8a one can recognize, in the position-encoded response of the sensor, 4 quadrants of alternating high and low voltage values arranged around the center point of the sensor. The localized heat source generates temperature gradients in the transducers both parallel and orthogonal to the sensor's surface, such that both the CSE and the TSE contribute to the measured voltage. CSE contributions are most prominent when the laser beam is positioned directly over an antimony transducer/tungsten wire junction, with the sign of the CSE voltage contribution dependent on the polarity of the junction (i.e., positive with antimony oriented towards the positive voltage terminal and tungsten towards the negative voltage terminal). This is highlighted in Fig. 8b by superimposing the laser scan results over the layout of the transducers and wires. The CSE contributions generate the 4 quadrants of alternating high and low voltage values on top of a gently and radially varying TSE voltage contribution. The positive sign of the measured voltage irrespective of heating probe location indicates that the voltage contributions from the TSE are larger in magnitude than those of the CSE, even in conditions tailored to enhance the CSE contributions. Therefore, these results validate the assertion that the TSE is the dominant transduction mechanism operating in the heat flux sensor under uniform heating conditions (i.e., when the temperature gradients are predominantly normal to the surface of the sensor).

The laser scan data also reveals that, along the symmetry axes of the

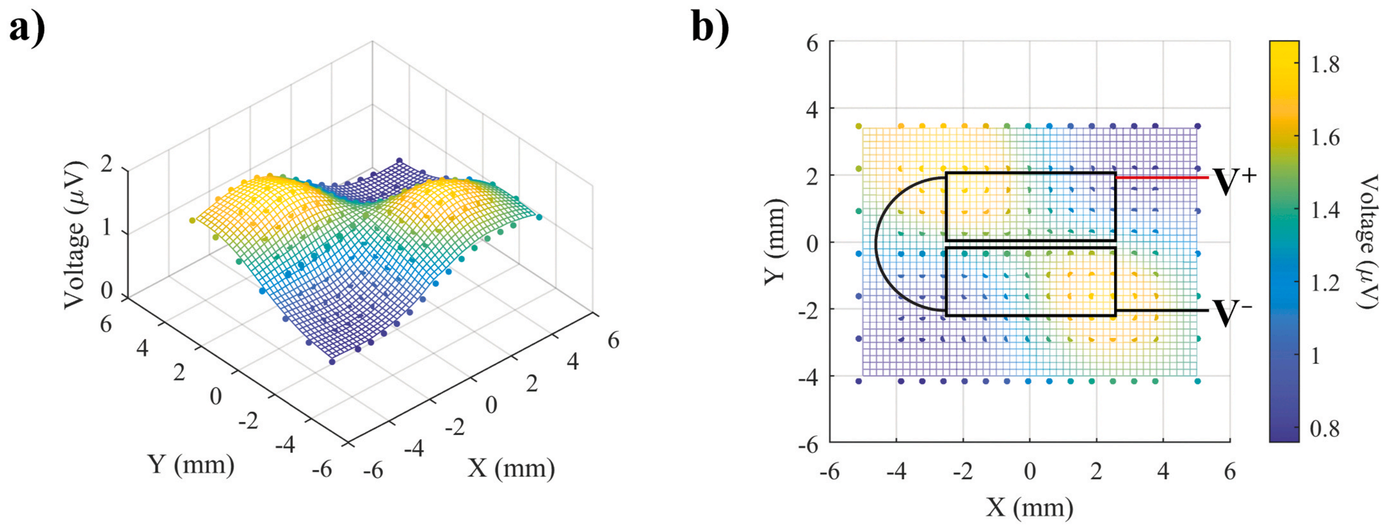

Fig. 8. Laser scan data. (a) Sensor response as a function of the position of the heating laser spot with respect to the center of the heat spreader. (b) Outline of the antimony prisms and the tungsten wiring overlayed with the laser scan data. The sensor response is presented using a color scale. Note that all the voltage values are positive.

TSE sensor, the TSE voltage decreases radially at a slow rate. The voltage decreases from the centroid value by an average of 20% at a distance of 5 mm from the center. In comparison, when performing the laser scan on the surface of the reference Medtherm 64–3–20 heat flux sensor, the voltage decreases by 50% at a distance of 1 mm from its center, and by more than 99.5% at a distance of 3 mm from the center. The design of the TSE sensor facilitates a high uniformity in sensor response over an area that far exceeds that of the transducers.

6. Conclusions

A heat flux sensor based on the transverse Seebeck effect in single crystal antimony demonstrated a linear transduction of the incident heat flux to an electrical voltage signal in the range of 0.06 – 7 W/cm^2, with even higher heat fluxes possible. The theoretically high responsivity of antimony and its stability over a wide range of environmental conditions make it a promising material for TSE-based sensors. Nevertheless, incorporating the antimony transducers into a rugged sensor package may be necessary and can have a significant impact on the sensor's performance parameters. The ruggedization of the heat flux sensor achieved design objectives that included improved stability, lower output noise, a larger active area, and a high degree of uniformity of the heat flux through the transducers. These benefits came at the cost of attenuating the heat flux through the transducers and increasing the sensor's time constant. Data from experiments and simulations illustrated how other performance-oriented design criteria could be met, for example, how to modify the package to produce a higher responsivity, shorten the transients in the response due to a sudden change in input value, or achieve a wider temperature range of operation. Compared to other heat flux sensing technologies, the design principles highlighted here are compatible with a wider range of materials and applications that target extreme high and extreme low temperatures.

Funding

This work was supported by the Department of Energy [grant DE-FE0031902].

CRediT authorship contribution statement

Kenneth McAfee: Methodology, Investigation, Data curation, Formal analysis, Writing – original draft, Writing – review & editing, Visualization. **Peter Sunderland:** Methodology, Writing – original draft, Writing – review & editing, Visualization, Supervision, Funding acquisition. **Oded Rabin:** Conceptualization, Methodology, Writing – original draft, Writing – review & editing, Visualization, Supervision, Funding acquisition.

Declaration of Competing Interest

The authors declare that they have no known competing financial interests or personal relationships that could have appeared to influence the work reported in this paper.

Data Availability

Data available upon request.

Acknowledgements

We acknowledge the support of the Maryland NanoCenter and its AIMLab. We thank Nolan Ballew, Dr. Don Schmadel, and Tom Weimar for the design and the fabrication of calibration system components.

References

[1] P.R.N. Childs, J.R. Greenwood, C.A. Long, Heat flux measurement techniques, Proc. Inst. Mech. Eng., Part C: J. Mech. Eng. Sci. 213 (1999) 655–677, https://doi.org/10.1177/095440629921300702.
[2] R.A. Miller, H.S. Alpert, Temperature dependent performance of Schmidt–Boelter heat flux sensors, Rev. Sci. Instrum. 94 (2023), 025002, https://doi.org/10.1063/5.0129703.
[3] H.J. Goldsmid, Application of the transverse thermoelectric effects, J. Electron. Mater. 40 (2011) 1254–1259, https://doi.org/10.1007/s11664-010-1357-3.
[4] Y. Tang, B. Cui, C. Zhou, M. Grayson, p × n-type transverse thermoelectrics: a novel type of thermal management material, J. Electron. Mater. 44 (2015) 2095–2104, https://doi.org/10.1007/s11664-015-3666-z.
[5] K.F. Renk, J. Betz, S. Zeuner, H. Lengfellner, W. Prettl, Thermopile effect due to laser radiation heating in thin films of high-Tc materials, Phys. C: Superconductivity 235–240 (1994) 37–40, https://doi.org/10.1016/0921-4534(94)91308-0.
[6] T. Roediger, H. Knauss, U. Gaisbauer, E. Kraemer, S. Jenkins, J. von Wolfersdorf, Time-resolved heat transfer measurements on the tip wall of a ribbed channel using a novel heat flux sensor—part I: sensor and benchmarks, J. Turbomach. 130 (2008), 011018, https://doi.org/10.1115/1.2751141.
[7] T. Kanno, K. Takahashi, A. Sakai, H. Tamaki, H. Kusada, Y. Yamada, Detection of thermal radiation, sensing of heat flux, and recovery of waste heat by the transverse thermoelectric effect, J. Electron. Mater. 43 (2014) 2072–2080, https://doi.org/10.1007/s11664-013-2959-3.

[8] S.Z. Sapozhnikov, V.Yu Mityakov, A.V. Mityakov, Bismuth-based gradient heat-flux sensors in thermal experiment, High. Temp. 42 (2004) 629–638, https://doi.org/10.1023/B:HITE.0000039993.76288.01.

[9] M.R. Scudder, B. He, Y. Wang, A. Rai, D.G. Cahill, W. Windl, J.P. Heremans, J. E. Goldberger, Highly efficient transverse thermoelectric devices with Re_4Si_7 crystals, Energy Environ. Sci. 14 (2021) 4009–4017, https://doi.org/10.1039/D1EE00923K.

[10] M.R. Scudder, K.G. Koster, J.P. Heremans, J.E. Goldberger, Adiabatic and isothermal configurations for Re_4Si_7 transverse thermoelectric power generators, Appl. Phys. Rev. 9 (2022), 021420, https://doi.org/10.1063/5.0073354.

[11] Th Zahner, R. Förg, H. Lengfellner, Transverse thermoelectric response of a tilted metallic multilayer structure, Appl. Phys. Lett. 73 (1998) 1364–1366, https://doi.org/10.1063/1.122376.

[12] A.V. Mityakov, S.Z. Sapozhnikov, V.Y. Mityakov, A.A. Snarskii, M.I. Zhenirovsky, J.J. Pyrhönen, Gradient heat flux sensors for high temperature environments, Sens. Actuators A Phys. 176 (2012) 1–9, https://doi.org/10.1016/j.sna.2011.12.020.

[13] A. Kyarad, H. Lengfellner, Al–Si multilayers: a synthetic material with large thermoelectric anisotropy, Appl. Phys. Lett. 85 (2004) 5613–5615, https://doi.org/10.1063/1.1830680.

[14] T. Meier, P. Stathopoulos, Ph.R. Von Rohr, Design and convective calibration of a transverse heat flux sensor, Exp. Heat. Transf. 29 (2016) 139–150, https://doi.org/10.1080/08916152.2014.945050.

[15] T. Kanno, S. Yotsuhashi, A. Sakai, K. Takahashi, H. Adachi, Enhancement of transverse thermoelectric power factor in tilted Bi/Cu multilayer, Appl. Phys. Lett. 94 (2009), 061917, https://doi.org/10.1063/1.3081411.

[16] W. Zhu, H. Zhou, P. Wei, C. Sun, D. He, X. Nie, X. Sang, W. Zhao, Q. Zhang, High-throughput optimization and fabrication of $Bi_2Te_{2.7}Se_{0.3}$-based artificially tilted multilayer thermoelectric devices, J. Eur. Ceram. Soc. 42 (2022) 3913–3919, https://doi.org/10.1016/j.jeurceramsoc.2022.03.034.

[17] W. Zhu, X. Guo, X. Sang, P. Wei, X. Nie, W. Zhao, Q. Zhang, Fabrication and performance prediction of $Ni/Bi_{0.5}Sb_{1.5}Te_3$ artificially-tilted multilayer devices with transverse thermoelectric effect, J. Power Sources 512 (2021), 230471, https://doi.org/10.1016/j.jpowsour.2021.230471.

[18] K. Uchida, J.P. Heremans, Thermoelectrics: from longitudinal to transverse, Joule 6 (2022) 2240–2245, https://doi.org/10.1016/j.joule.2022.08.016.

[19] J. Xiang, S. Hu, M. Lyu, W. Zhu, C. Ma, Z. Chen, F. Steglich, G. Chen, P. Sun, Large transverse thermoelectric figure of merit in a topological Dirac semimetal, Sci. China Phys. Mech. Astron. 63 (2019), 237011, https://doi.org/10.1007/s11433-019-1445-4.

[20] W. Zhou, Y. Sakuraba, Heat flux sensing by anomalous Nernst effect in Fe–Al thin films on a flexible substrate, Appl. Phys. Express 13 (2020), 043001, https://doi.org/10.35848/1882-0786/ab79fe.

[21] K. Uchida, T. Nonaka, T. Yoshino, T. Kikkawa, D. Kikuchi, E. Saitoh, Enhancement of spin-Seebeck voltage by spin-hall thermopile, Appl. Phys. Express 5 (2012), 093001, https://doi.org/10.1143/APEX.5.093001.

[22] A. Sakai, T. Kanno, K. Takahashi, H. Tamaki, H. Kusada, Y. Yamada, H. Abe, Breaking the trade-off between thermal and electrical conductivities in the thermoelectric material of an artificially tilted multilayer, Sci. Rep. 4 (2014) 6089, https://doi.org/10.1038/srep06089.

[23] K. Yue, W. Zhu, Q. He, X. Nie, X. Qi, C. Sun, W. Zhao, Q. Zhang, High transverse thermoelectric performance and interfacial stability of $Co/Bi_{0.5}Sb_{1.5}Te_3$ artificially tilted multilayer thermoelectric devices, ACS Appl. Mater. Interfaces 14 (2022) 39053–39061, https://doi.org/10.1021/acsami.2c10227.

[24] Z. Liu, S. Liu, J. Zhao, Y. Yue, Q. Xu, F. Yang, A transient heat flux sensor based on the transverse Seebeck effect of single crystal Bi_2Te_3, Measurement 198 (2022), 111419, https://doi.org/10.1016/j.measurement.2022.111419.

[25] K. Takahashi, A. Sakai, T. Kanno, H. Adachi, Tailoring of inclined crystal orientation in layered cobaltite thin films for the development of off-diagonal thermoelectric effect, Appl. Phys. Lett. 95 (2009), 051913, https://doi.org/10.1063/1.3194796.

[26] P.X. Zhang, H.-U. Habermeier, Atomic layer thermopile materials: physics and application, J. Nanomater. 2008 (2008), e329601, https://doi.org/10.1155/2008/329601.

[27] G. Yang, L. Zhang, Laser induced thermoelectric voltage effect of $Bi_{2.1}Sr_{1.9}CaCu_2O_8$ thin films, in: International Photonics and OptoElectronics Meetings (2014), Paper JF2A.41, Optica Publishing Group, 2014, https://doi.org/10.1364/FBTA.2014.JF2A.41.

[28] S. Heinze, Thermoelectric properties of oxide heterostructures, Doctoral Thesis, University of Stuttgart (2013), doi:10.18419/opus-6836.

[29] X. Chen, B. Tao, R. Zhao, K. Yang, Y. Xia, Z. Li, T. Xie, Y. Zhong, T. Zhang, High-frequency response heat flux sensor based on the transverse thermoelectric effect of inclined $La_{1-x}Ca_xMnO_3$ films, Appl. Phys. Lett. 121 (2022), 204102, https://doi.org/10.1063/5.0124140.

[30] S. Song, Y. Wang, L. Yu, Highly sensitive heat flux sensor based on the transverse thermoelectric effect of $YBa_2Cu_3O_{7-\delta}$ thin film, Appl. Phys. Lett. 117 (2020), 123902, https://doi.org/10.1063/5.0021451.

[31] X. Chen, B. Tao, R. Zhao, K. Yang, Z. Li, T. Xie, Y. Zhong, T. Zhang, Y. Xia, The atomic layer thermopile heat flux sensor based on the inclined epitaxial $YBa_2Cu_3O_{7-\delta}$ films, Mater. Lett. 330 (2023), 133336, https://doi.org/10.1016/j.matlet.2022.133336.

[32] W.M. Yim, A. Amith, Bi-Sb alloys for magneto-thermoelectric and thermomagnetic cooling, Solid-State Electron. 15 (1972) 1141–1165, https://doi.org/10.1016/0038-1101(72)90173-6.

[33] C.Y. Ho, R.W. Powell, P.E. Liley, Thermal conductivity of the elements, J. Phys. Chem. Ref. Data 1 (1972) 279–421, https://doi.org/10.1063/1.3253100.

[34] W.M. Pitts, A.V. Murthy, J.L. de Ris, J.-R. Filtz, K. Nygård, D. Smith, I. Wetterlund, Round robin study of total heat flux gauge calibration at fire laboratories, Fire Safety J 41 (2006) 459–475, https://doi.org/10.1016/j.firesaf.2006.04.004.

[35] A.V. Murthy, B.K. Tsai, R.D. Saunders, Radiative calibration of heat-flux sensors at NIST: Facilities and techniques, J. Res. Natl. Inst. Stand. Technol. 105 (2000) 293, https://doi.org/10.6028/jres.105.033.

[36] N. Cholewa, P.T. Summers, S. Feih, A.P. Mouritz, B.Y. Lattimer, S.W. Case, A technique for coupled thermomechanical response measurement using infrared thermography and digital image correlation (TDIC), Exp. Mech. 56 (2016) 145–164, https://doi.org/10.1007/s11340-015-0086-1.

[37] H. Kim. Procedures to obtain accurate measurement from a gas fueled burner, Masters Thesis, University of Maryland (2014), https://doi.org/10.13016/M2F02F. http://hdl.handle.net/1903/16227.

[38] G.A. Saunders, C. Miziumski, G.S. Cooper, A. Lawson, The Seebeck coefficients of antimony and arsenic single crystals, J. Phys. Chem. Solids 26 (1965) 1299–1303, https://doi.org/10.1016/0022-3697(65)90112-5.

[39] O.J. Pountney, M. Patinios, H. Tang, D. Luberti, C.M. Sangan, J.A. Scobie, J. M. Owen, G.D. Lock, Calibration of thermopile heat flux gauges using a physically-based equation, Proc. Inst. Mech. Eng., Part A: J. Power Energy 235 (2021) 1806–1816, https://doi.org/10.1177/0957650920982103.

[40] C.A. Pullins, T.E. Diller, In situ high temperature heat flux sensor calibration, Int. J. Heat. Mass Transf. 53 (2010) 3429–3438, https://doi.org/10.1016/j.ijheatmasstransfer.2010.03.042.

[41] J.R. Trelewicz, J.P. Longtin, D.O. Hubble, R.J. Greenlaw, High-temperature calibration of direct write heat flux sensors from 25 °C to 860 °C using the in-cavity radiation method, IEEE Sens. J. 15 (2015) 358–364, https://doi.org/10.1109/JSEN.2014.2343931.

[42] G.A. Saunders, Ö. Öktü, The Seebeck coefficient and the Fermi surface of antimony single crystals, J. Phys. Chem. Solids 29 (1968) 327–333, https://doi.org/10.1016/0022-3697(68)90077-2.

[43] N.E. Hager Jr., Thin foil heat meter, Rev. Sci. Instrum. 36 (1965) 1564–1570, https://doi.org/10.1063/1.1719394.

Kenneth McAfee: PhD Student in Aerospace Engineering and NASA Space Technology Research Fellow at the University of Maryland, College Park (MD, USA). He earned his BS and MS in Mechanical Engineering from Binghamton University (SUNY). His research focuses on the development of thermoelectric heat flux measurement systems and their application in extreme environments.

Peter Sunderland: Professor, Department of Fire Protection Engineering, the University of Maryland. He earned his PhD in Aerospace Engineering at the University of Michigan. His research interests are in combustion and fire dynamics, including heat flux measurement, soot formation and oxidation, pyrometry, laminar diffusion flames, microgravity combustion, and fires involving firebrands, refrigerants, hydrogen, highway vehicles, and spacecraft.

Oded Rabin: Associate Professor of Materials Science and Engineering at the University of Maryland, College Park (MD, USA). He earned his PhD in Physical Chemistry at the Massachusetts Institute of Technology in 2004. His research focuses on nanofabrication, characterization and theory of materials for Plasmonics and Thermoelectrics. He was awarded the US Scholar Fulbright fellowship (2022–2023) for fostering international collaborations in the science and technology of transverse thermoelectrics.